Building and Environment 294 (2026) 114359

Contents lists available at ScienceDirect

Building and Environment

journal homepage: www.elsevier.com/locate/buildenv

Comparative assessment of quantitative infrared thermography approaches for experimental thermal transmittance determination using UAVs

Marta Videras-Rodríguez, Victoria Patricia López-Cabeza, Sergio Gómez-Melgar *, José Manuel Andújar-Márquez

Research Centre for Technology, Energy and Sustainability (CITES), Universidad de Huelva, Huelva, Spain

ARTICLE INFO

Keywords:
Thermal transmittance
U-value
Aerial thermography
Unmanned aerial vehicles
Drones
Building envelope
Envelope characterization

ABSTRACT

Rapid and non-contact evaluation of building thermal efficiency remains a major challenge in urban energy management. The increasing use of Unmanned Aerial Vehicles (UAVs) equipped with thermal cameras has expanded the potential of aerial thermography as a diagnostic tool for assessing building energy performance. This study compares five Quantitative Infrared Thermography (QIRT) methodologies (Methods A-E) for estimating the U-value of building envelopes, benchmarking them against theoretical reference values derived from in-situ wall characterization. The research analyzes the sensitivity of these methods to boundary condition uncertainties through two winter experimental campaigns in southwestern Spain. Results reveal that no single experimental method is universally robust; accuracy is critically dependent on the algebraic formulation of each method and specific environmental variables. Methods A and B exhibited extreme sensitivity to wind speed, showing deviations of up to 52 % with minor perturbations (±1 m/s), rendering them unsuitable without precise anemometry. Method E showed deviations of ≈40 % linked to internal surface temperature variations, while Method C proved highly volatile regarding external surface temperatures. Conversely, Method D, which incorporates both convective and radiative terms, emerged as the most balanced approach, showing intermediate stability (≈20– 27 % deviation) across all variables. Consequently, this study identifies the optimal application scenarios for each method based on field measurement capabilities, providing a decision-making framework to ensure the reliability of UAV-based thermographic assessments.

1. Introduction

Improving the energy performance of the building stock is an essential imperative for climate change mitigation, given that the sector accounts for approximately 40 % of energy consumption and 36 % of greenhouse gas emissions in the European Union [1]. Since 85 % of European buildings pre-date the year 2000 and 75 % exhibit poor thermal performance [2], current policies prioritize renovation over new construction. However, the effectiveness of these interventions relies on a reliable assessment of the thermal envelope, which is responsible for a significant portion of energy losses through transmission, infiltration, and thermal bridges [3–8].

The fundamental indicator for this assessment is thermal transmittance (U-value) [9]. Although the theoretical method standardized in ISO 6946 [10] allows for its calculation during the design phase, its application to existing buildings is problematic. Uncertainty regarding the actual composition of building assemblies, variability in material conductivity, and the effects of aging lead to significant discrepancies between theoretical values and actual performance [11–13].

To overcome this uncertainty, research has increasingly focused on refining in situ methods for estimating the U-value [14–19]. Among the most established techniques are the Heat Flow Meter (HFM) method, standardized in ISO 9869– 1 [20]; the Thermometric Method (THM), widely applied in research; and Quantitative Infrared Thermography (QIRT), regulated by ISO 9869– 2 [21]. Despite their instrumental differences, these approaches converge on two critical operational challenges: first, the dependence on quasi-steady-state environmental conditions, which necessitates prioritizing winter and nighttime measurements with a high thermal gradient ($\Delta T > 10$ °C) [22–25]; and second, the disparity in execution times, where QIRT reduces tests that require days or weeks with contact-based techniques to just a few hours [17,26].

* Corresponding author.
E-mail addresses: marta.videras@pi.uhu.es (M. Videras-Rodríguez), victoria.lopez@pi.uhu.es (V.P. López-Cabeza), sergio.gomez@dimme.uhu.es (S. Gómez-Melgar), andujar@diesia.uhu.es (J.M. Andújar-Márquez).

https://doi.org/10.1016/j.buildenv.2026.114359
Received 9 December 2025; Received in revised form 27 January 2026; Accepted 10 February 2026
Available online 14 February 2026

Despite the robustness of these methods under controlled conditions, their application in high-rise, large-scale, or hard-to-access existing buildings presents logistical limitations. It is within this context that the integration of thermographic cameras into Unmanned Aerial Vehicles (UAVs) has emerged as a disruptive solution to overcome barriers of accessibility and scale [27–33].

While its qualitative use for the detection of building pathologies is widely established [34–36], the quantitative estimation of U-value via UAVs (UAV-QIRT) remains an open field of research. Unlike indoor thermography, where environmental conditions can be considered controlled [37–42], outdoor measurement faces the complexity of modeling heat exchange under variable wind and radiation conditions. The lack of a unified physical model has led to a considerable diversity of methodological approaches, which can be categorized according to their physical formulation.

A first group of methodologies prioritizes the simplification of physical variables to maximize operational efficiency during rapid inspections, assuming certain constants compared to integral models, as seen in the proposals by Dall'O et al. (2013) [43] and Bayomi et al. (2021) [44]. In particular, Dall'O et al [43] establish the equivalence between the heat flow through the building envelope and the convective flow at the exterior surface, neglecting the radiative contribution. Conversely, Bayomi et al [44] propose a linearized radiative-convective model that relies on fixed convection coefficients rather than dynamic wind measurements. Despite their differences in formulation, both methodologies share a clear screening orientation, allowing for non-invasive diagnoses within short operational windows.

In contrast, a second group of studies advocates for analytical rigor based on the thermal balance relationship between the interior and exterior of the envelope. This line of research, consolidated by the proposal of Albatici et al. (2010, 2015) [45,46] for terrestrial thermography, is distinguished by the explicit integration of radiative and convective components in the heat flow calculation. Its main methodological contribution lies in minimizing systematic error by using the thermal camera for the in-situ determination of critical radiometric parameters (surface temperature, reflected temperature, and emissivity), avoiding the use of theoretical values.

The translation of this integral approach to aerial platforms has driven recent adaptations aimed at overcoming accessibility barriers. Benz et al. (2021) [47] adopt this integral formulation for application via drones, adjusting the thermal variables of the original equation. Their proposal is notable for its capacity to populate BIM models with information on the complete building envelope in reduced times. As an evolution of this line, Zhang et al. (2024) [48] propose an optimized radiative model that refines accuracy by decomposing radiative transfer into three independent components (sky, air, and ground). However, while these aerial methods maintain physical rigor, the literature suggests that their implementation introduces new operational complexities.

To systematize the analysis, these approaches have been categorized as Methods A through E. Table 1 summarizes their technical characteristics, experimental validation, and identified operational limitations.

This disparity in formulations, ranging from rapid convective simplifications to complex radiative balances, creates significant uncertainty regarding the real-world applicability of each method under flight conditions, where critical variables such as wind and thermal stability fluctuate dynamically. To date, the literature lacks a systematic comparison evaluating these five approaches under identical experimental conditions to quantify their sensitivity and robustness.

The present work addresses this scientific gap by comparing the described methodologies (A–E) against the standardized theoretical calculation (ISO 6946). The main novelty of the study lies in the simultaneous evaluation of the four cardinal orientations on the same building, thereby ensuring homogeneity in measurement conditions. The ultimate objective is to determine the validity and operational limits of each approach, providing clear criteria to select the most suitable method for reliable thermal characterization using aerial technology.

Table 1
Structured review of existing methods: experimental validation, reported accuracy, and operational limitations.

ID	Reference	Experimental validation	Accuracy and findings	Limitations and testing conditions
A	Dall'O et al. (2013) [43]	Terrestrial. 14 buildings. 2–3 h campaigns in winter.	Reliable on massive walls with high thermal inertia. Rapid non-invasive diagnosis.	Error > 50 % on facades with external thermal insulation. Requires climatic stability. Sensitive to wind.
B	Albatici et al. (2010, 2015) [45, 46]	Terrestrial. 30-minute campaigns over 3 winters.	Reliable on massive walls with high thermal inertia.	Limitations on lightweight or super-insulated envelopes.
			In-situ measurement of radiative factors.	Strict climatic requirements: winter and $\Delta T > 15$ °C. Critical influence of wall solar orientation.
C	Benz et al. (2021) [47]	Aerial/UAV. 10-minute inspection at sunrise.	Record-time BIM integration (vertical and horizontal envelopes).	Aerial spatial resolution lower than manual inspection.
				Critical time window (sunrise) due to visibility and solar load.
D	Zhang et al. (2024) [48]	Aerial/UAV. 10-minute campaigns at sunset (winter).	Error < 2 % compared to contact methods.	Method accuracy sensitive to flight parameters.
			Definition of UAV operational protocol.	Requires: Capture distance < 15 m Flight speed < 0.5 m/s Wind speed < 0.4 m/s
E	Bayomi et al. (2021) [44]	Aerial/UAV. 2-hour inspection at sunrise (spring).	Useful for calibrating simulation models (deviations reduced from 21 % to 0.9 %).	Method reliability conditioned by environmental stability (overcast skies and calm wind). Requires precise measurement of indoor thermal conditions.

The research was conducted on a university building in southwestern Spain. Data collection combined fixed sensors and a UAV-mounted infrared camera to measure air and surface temperatures, alongside wind speed. Two 60-minute winter campaigns were executed pre-dawn to minimize solar radiation and maximize thermal contrast; indoor data were recorded at one-minute intervals, while exterior UAV acquisition occurred every ten minutes.

In-situ inspections characterized the envelope materials to determine theoretical U-values for comparison. To assess reliability, a univariate sensitivity analysis was performed by recalculating U-values under controlled perturbations, quantifying the relative influence of each input variable. The findings support specific recommendations for effective UAV deployment, highlighting the critical necessity of analyzing each facade orientation independently for accurate thermal characterization. The paper is organized as follows: Section 2 details materials and methodology; Section 3 presents results; Section 4 discusses findings; and Section 5 offers conclusions.

2. Materials and methods

2.1. Case study

The research was conducted at the building of the Centre for Research in Technology, Energy and Sustainability (CITES), located on the La Rábida Campus of the University of Huelva (SW Spain) (Fig. 1). The area is classified as Csa under the Köppen-Geiger system [49], characterized by a subtropical Mediterranean climate with significant Atlantic influence.

Built in 1962 and renovated in the 2000s, the building features a square layout around a central courtyard, flanked by two towers that characterize its two-story structure. The envelope consists of multilayer masonry walls retrofitted with thermal insulation. Experimental measurements were carried out on the upper floor across all four cardinal orientations.

2.2. Data acquisition and post-processing

The data acquisition strategy comprised two stages: geometric and material characterization to establish the theoretical baseline, and experimental campaigns using in-situ sensors and aerial thermography. Notably, the experimental phase preceded the physical inspection to preserve the envelope's thermal properties.

An in-situ inspection by means of sampling was conducted to identify the envelope stratigraphy and measure layer thicknesses (Fig. 2). The inspection revealed a relatively homogeneous configuration across all orientations, consisting of an external cement mortar render, a double hollow brick wall, expanded polystyrene (EPS) insulation combined with air cavities, and an internal mortar layer. The primary variations were observed in the insulation thickness and air cavity depths: the North façade incorporated 0.04 m of EPS compared to 0.02 m in the other orientations, with air cavity sizes also differing among façades. Consequently, the baseline for the theoretical U-value calculation was established by combining these in-situ geometric measurements with standard thermal conductivity values obtained from the Spanish Technical Building Code (CTE), as detailed in Table 2.

Regarding the experimental campaign for the thermographic analysis (Fig. 3), the measurements were carried out for 60 min before dawn on two winter days in February (Trial 1) and March (Trial 2), following literature recommendations to minimize the influence of direct solar radiation [43,45,46]. To ensure a sufficient thermal gradient, targeting a minimum indoor-outdoor temperature difference of 10 °C ($\Delta T > 10$ °C), the heating systems were activated the day before the experiment.

During the experiment, data was acquired simultaneously inside and outside the north, east, south, and west façades. Inside, air and wall surface temperatures were recorded every minute using four Testo 176-H1 data loggers, each equipped with ambient and surface NTC temperature probes installed away from direct heating sources. On the exterior, data acquisition was performed using a KIMO LV 130S thermal anemometer to measure air temperature and wind speed, and a DJI Mavic 2 Enterprise Advanced UAV, equipped with a radiometric thermal camera, to capture surface and reflected temperatures. Table 3 specifies and details the equipment used during the experimental campaign.

Regarding the data capture protocol, flight missions were performed manually, ensuring strict control over the variables affecting thermal accuracy as highlighted in recent studies [50]. To eliminate motion blur and errors resulting from flight speed, the UAV was operated in a 'stop-and-go' mode: the aircraft was positioned and stabilized in a hovering state (speed ≈ 0 m/s) prior to each image capture. Spatially, the device maintained approximately 5 m to minimize atmospheric attenuation and a perpendicular viewing angle to avoid reflections. Given the manual nature of the flight, the protocol prioritized consistent framing to ensure that the façade areas under study were fully captured in every sequence, rather than adhering to a fixed photogrammetric overlap percentage. Finally, regarding temporal resolution and coverage, images were acquired at 10-minute intervals over the 60-minute duration of the experiment, which required the use of three batteries per mission.

In the post-processing phase, the analysis of the thermal images was carried out using the DJI Thermal Analysis Tool v.3 software, which enabled the processing of a total of 48 images (Fig. 4).

From these images, data on the exterior surface temperature were obtained, by defining specific Regions of Interest (ROIs) on the opaque areas of the façade, corresponding to the points where the surface temperature had previously been measured from the interior. Finally, to ensure measurement reliability, the analysis parameters were configured with a sensor-to-wall distance of 5 m, an emissivity of 0.94, and the reflected apparent temperature calculated via the diffuse reflector method according to ISO 18 , 434 – 1 [51].

2.3. U-Value calculation

Once the information was post-processed, the calculation of the U-values for the different façades of the building, following different methodologies, was carried out. The U-value is defined as the heat flux per unit area, q (W/m^2), divided by the temperature difference between the two environments separated by the envelope: T_i and T_o (K), which are the interior and exterior air temperatures, respectively (Eq. 1).

$$U - value = \frac{q}{(T_i - T_o)} \frac{\mathrm{W}}{\mathrm{m^2K}} \tag{1}$$

For theoretical calculation, ISO 6946 [10] calculates the U-value as the inverse of the total thermal resistance, R, of the material comprising the envelope (Eq. 2).

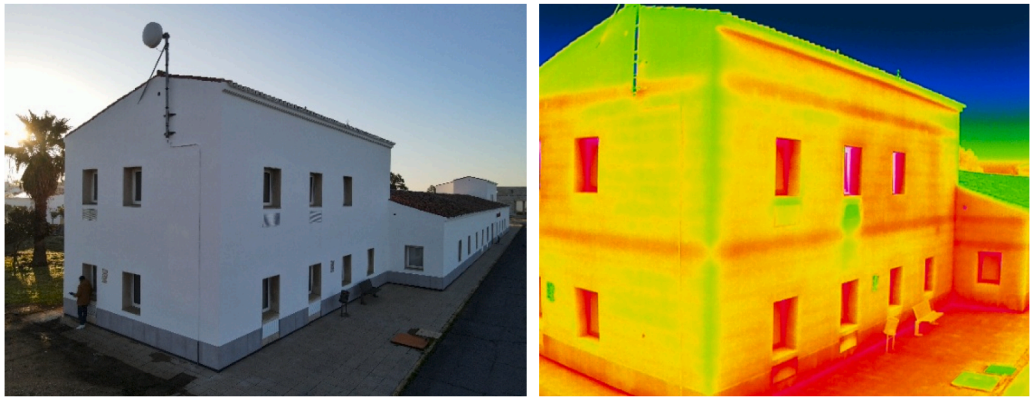

Fig. 1. Research Centre for Technology, Energy and Sustainability (CITES).

Fig. 2. In-situ envelope inspection by means of sampling: a) North, b) South, c) East, d) West Façades.

Table 2
Internal envelope characterization (from top to bottom, from outside to inside).

Façade	Material	Thickness (m)	Thermal Conductivity (W/mK)
North	Cement Mortar	0.02	0.7
	Double hollow brick wall	0.26	0.432
	Cement Mortar	0.02	0.7
	Expanded Polystyrene (EPS)	0.04	0.0375
	Air cavity	0.055	-
	Gypsum Plaster	0.015	0.3
South	Cement Mortar	0.02	0.7
	Double hollow brick wall	0.26	0.432
	Cement Mortar	0.02	0.7
	Expanded Polystyrene (EPS)	0.02	0.0375
	Air cavity	0.075	-
	Gypsum Plaster	0.015	0.3
East	Cement Mortar	0.02	0.7
	Double hollow brick wall	0.26	0.432
	Cement Mortar	0.02	0.7
	Air cavity	0.015	-
	Expanded Polystyrene (EPS)	0.02	0.0375
	Air cavity	0.065	-
	Gypsum Plaster	0.015	0.3
West	Cement Mortar	0.02	0.7
	Double hollow brick wall	0.26	0.432
	Cement Mortar	0.02	0.7
	Expanded Polystyrene (EPS)	0.02	0.0375
	Air cavity	0.055	-
	Gypsum Plaster	0.015	0.3

$$U-value = \frac{1}{R} = \frac{1}{R_{si} + \sum \frac{s_i}{\lambda_i} + R_{so}} \frac{W}{m^2K} \quad (2)$$

Where s_i and λ_i are the thickness and thermal conductivity, respectively, of each wall layer, and R_{si} and R_{so} are the internal and external thermal resistances of the surface. The resistances are determined from values provided by ISO 6946 and are based on specific boundary conditions related to convective and radiative heat transfer. For vertical façades, the standard recommends using $R_{si} = 0.13$ m²K/W and $R_{so} = 0.04$ m²K/W [10]. The theoretical U-value does not consider the elements related to heat transfer caused by convection and radiation, which changes with external wind speed and environmental temperature.

Consistent with the structured review presented in Section 1 (Table 1), this study quantitatively evaluates five distinct methodological approaches for estimating U-value from the building exterior. The following subsections detail the specific mathematical formulation governing each method, organizing them sequentially from the terrestrial baselines (Methods A and B) to the UAV-adapted procedures (Methods C, D, and E).

2.3.1. Method based on convective heat flux balance (Method A)

This method proposed by Dall'O et al [43], expresses the convective heat flux (q_{conv}), according to Newton's law of cooling, as a function of the convective heat transfer coefficient (h_c) and the temperature difference between the external wall surface (T_{so}) and the outdoor air temperature (T_o), as shown in Eq. 3:

$$q_{conv} = h_c \cdot (T_{so} - T_o) \frac{W}{m^2} \quad (3)$$

Dall'O et al. proposed a new formulation (Eq. 4) by combining Eq. 1 and Eq. 3:

$$U-value = h_c \cdot \frac{(T_{so} - T_o)}{(T_i - T_o)} \frac{W}{m^2K} \quad (4)$$

To calculate the convective heat transfer coefficient, h_c, the wind speed parameter (v) was considered by applying a simplified form of the Jürges equation (Eq. 5) [52].

$$h_c = 5.8 + 3.8054 \cdot v (v < 5m/s) \frac{W}{m^2K} \quad (5)$$

2.3.2. Method based on surface thermal balance (Method B)

Based on the surface thermal balance approach proposed by Albatici et al [45,46], this method assumes steady-state conditions where the heat flux dissipated at the exterior surface, q, is defined as the sum of the radiative (q_{rad}) and convective (q_{conv}) contributions. Consequently, the heat flux is formulated by combining the Stefan-Boltzmann law for radiation and Newton's law of cooling for convection, as expressed in Eq. 6:

$$q = \sigma \cdot \varepsilon \cdot \left(T_{so}^4 - T_o^4\right) + h_c \cdot (T_{so} - T_o) \frac{W}{m^2} \quad (6)$$

Where ε is the emissivity of the body and σ is the Stefan-Boltzmann constant ($5.67 \cdot 10^{-8}$ W/m²K⁴). For the convective heat transfer coefficient, h_c, Jürges' simplified formulation was adopted, assuming an air velocity approaching 0 m/s (< 1 m/s) near the wall surface. Integrating these parameters into the general transmittance equation, the U-value is finally determined by Eq. 7:

$$U-value = \frac{5.67 \cdot \varepsilon \cdot \left(\left(\frac{T_{SO}}{100}\right)^4 - \left(\frac{T_O}{100}\right)^4\right) + 3.8054 \cdot v \cdot (T_{so} - T_o)}{T_i - T_o} \frac{W}{m^2K} \quad (7)$$

2.3.3. UAV-based surface thermal balance method (Method C)

The mathematical formulation proposed by Benz et al [47] reformulates Eq. 7 by substituting air temperatures with surface temperatures (T_{si} and T_{so}) in the denominator. The U-value calculation is defined in Eq. 8:

$$U-value = \frac{\sigma \cdot \varepsilon \cdot \left(T_{so}^4 - T_o^4\right) + h_c \cdot (T_{so} - T_o)}{(T_{si} - T_{so})} \frac{W}{m^2K} \quad (8)$$

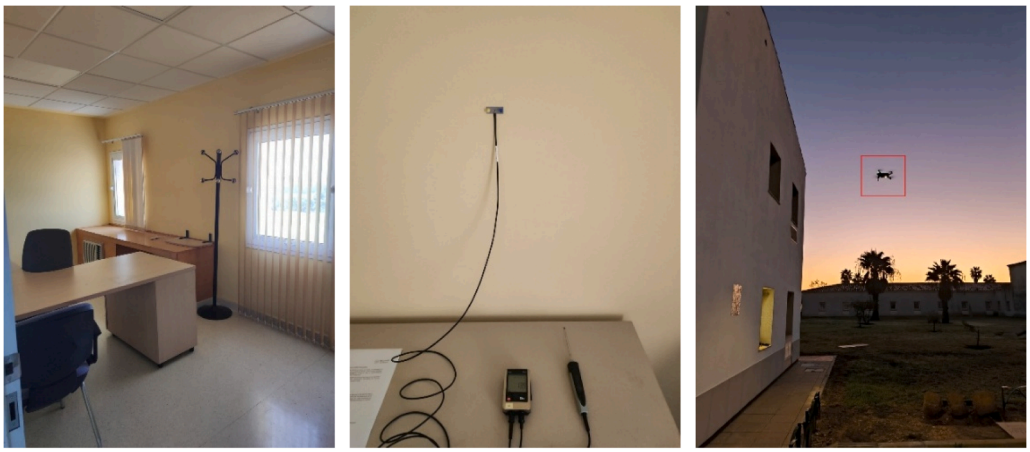

a) b) c)

Fig. 3. Data acquisition: a) Interior space of the building, b) Data acquisition from temperature indoor sensors, c) Exterior aerial inspection.

Table 3
Equipment specifications.

Equipment	Specifications	
176-H1 data logger (Testo) 	Measuring range	-20 to +70 ºC
	Weight	220 g
	Dimensions	103 x 63 x 33 mm
	Storage capacity	2.000.000 values
Ambient temperature probe (NTC) (Testo) 	Measuring range	-50 to +125 ºC
	Accuracy	±0.2 °C
	Response time	60 s
	Weight	104 g
Surface temperature probe (NTC) (Testo) 	Measuring range	-50 to +80 ºC
	Accuracy	±0.2 °C
	Response time	20 s
	Weight	60 g
Thermal anemometer KIMO LV 130S 	Measuring range (wind)	0.3 to 35 m/s
	Measuring range (temperature)	0 to +50 ºC
	Accuracy (wind)	±3% of reading ±0.1 m/s
	Accuracy (temperature)	±0.4% of reading ±0.3 °C
	Weight	390 g
	Vane diameter	Ø 100 mm
UAV DJI Mavic 2 Enterprise Advanced 	Measuring range (IR sensor)	-50 to +125 ºC
	Spectral range (IR sensor)	8-14 μm
	IR sensor resolution	640 x 512 (30 Hz)
	Accuracy (IR sensor)	±2 °C or ±2 %
	Take-off weight	909 g
	Dimensions (unfolded)	322 x 242 x 114 mm
	Max autonomy	31 min

Regarding the convective coefficient (h_c), which was not specified in the original proposal, an estimation based on the ISO 6946 standard [10] was adopted. Although the standard defines a total surface heat transfer coefficient of $h_e = 25$ W/m^{2}K (corresponding to $R_{so} = 0.04$ m^{2}K/W), this value aggregates both radiation and convection. Given that the present equation explicitly computes the radiative term, the

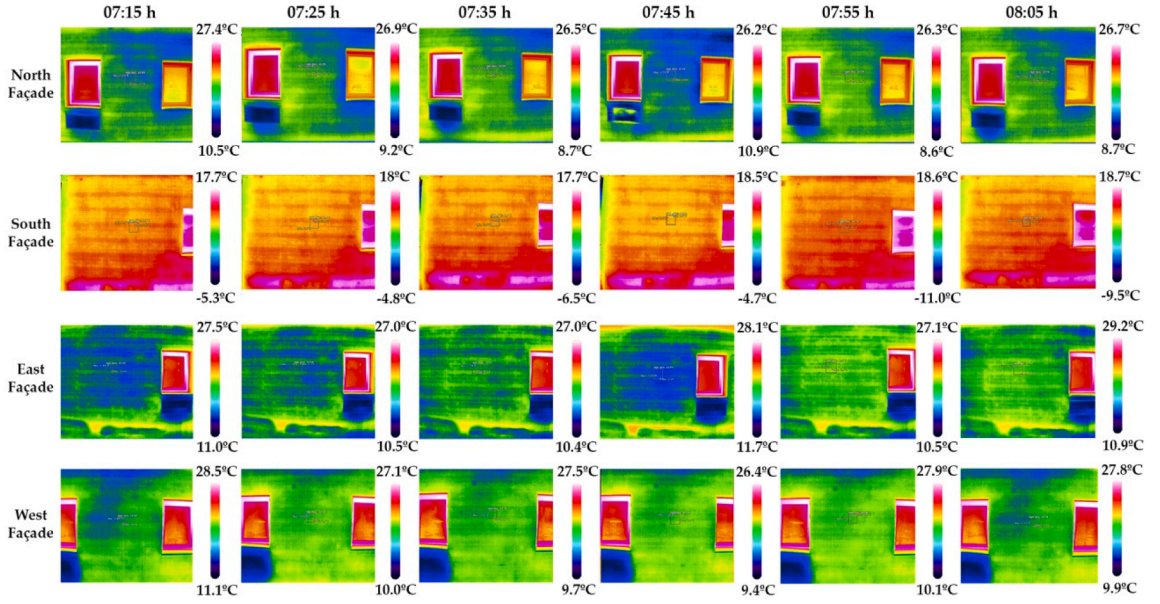

a)

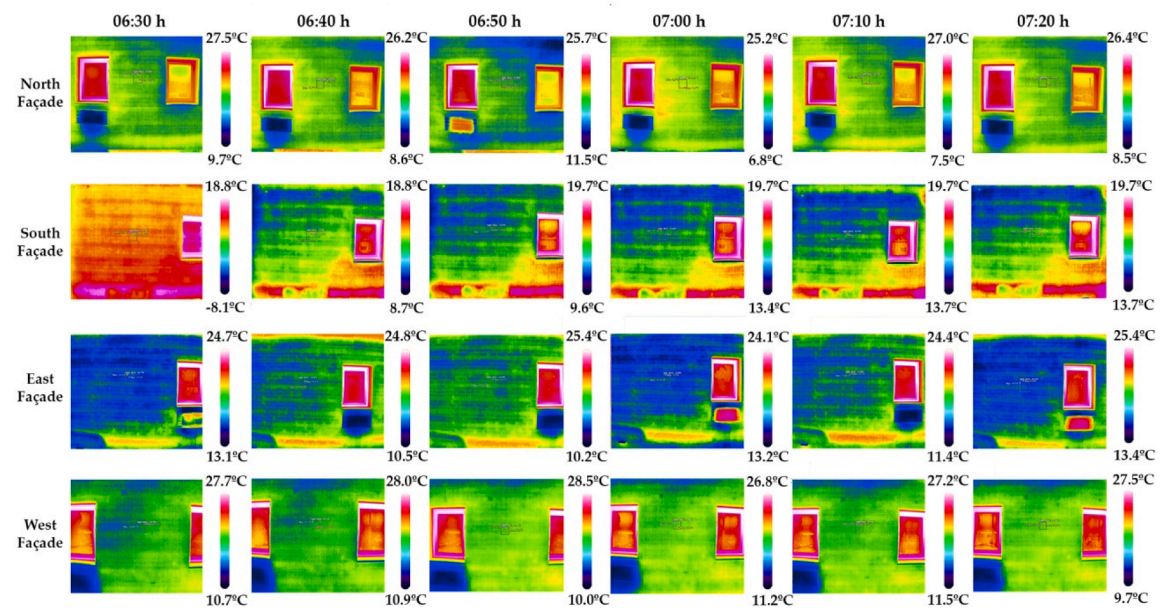

b)

Fig. 4. Data post-processing. Infrared images taken at 10 min of the different façades before dawn in two different days: a) Trial 1, b) Trial 2.

convective component was isolated, resulting in the adoption of a fixed value of $h_c \approx 10$ W/m^{2}K, which is consistent with low air velocity conditions.

2.3.4. Method based on multi-component radiative heat transfer (Method D)

The model proposed by Zhang et al [48] expands the thermal balance by decomposing the radiative component into three independent interactions with the sky, the air, and the ground. The resulting U-value formulation integrates the radiative heat transfer coefficients (h_r) for each medium alongside the convective component, as expressed in Eq. 9:

$$U-value = \frac{hr_{sky}\cdot(T_{so}-T_{sky}) + hr_{air}\cdot(T_{so}-T_o) + hr_{ground}\cdot(T_{so}-T_{ground}) + h_c\cdot(T_{so}-T_o)}{(T_i-T_o)} \frac{\mathrm{W}}{\mathrm{m^2K}} \quad (9)$$

Where $hr_{,sky}$, $hr_{,air}$ and $hr_{,ground}$ represent the radiative heat transfer coefficients for the sky, outdoor air, and ground, respectively. These are calculated using the generalized formulation in Eq. 10, where the subscript i denotes the specific medium (sky, air, or ground):

$$hr_i = \frac{\sigma \cdot \varepsilon \cdot F_i \cdot \left(T_{so}^4 - T_i^4\right)}{\left(T_{so} - T_i\right)} \frac{\mathrm{W}}{\mathrm{m^2K}} \tag{10}$$

T_{sky}, T_o y T_{ground} represent the temperatures of the sky, air, and ground. The ground temperature is assumed to be equal to the outdoor air temperature, and the sky temperature is calculated as a function of the air temperature and the sky emissivity (ε_{sky}) (Eq. 11).

$$T_{sky} = T_o \cdot \varepsilon_{sky}^{0.25} \mathrm{K} \tag{11}$$

F_{sky}, F_{air} y F_{ground} are the radiation angle factors for the exterior surface of the building with respect to the sky, the outdoor air, and the ground. These are determined based on α, which represents the angle between the building envelope and the horizontal plane (expressed in degrees), as defined in Eqs. 12– 14:

$$F_{sky} = 0.5 \cdot (1 + \cos\alpha) \cdot \cos\frac{\alpha}{2} \tag{12}$$

$$F_{air} = 0.5 \cdot (1 + \cos\alpha) \cdot \left(1 - \cos\frac{\alpha}{2}\right) \tag{13}$$

$$F_{ground} = 0.5 \cdot (1 - \cos\alpha) \tag{14}$$

Finally, the convective coefficient h_c is calculated using the simplification of the Jürges equation (Eq. 5).

2.3.5. Method based on linearized radiative–convective heat transfer (Method E)

The linearized model proposed by Bayomi et al [44] modifies the approach by Madding et al. (2008) [37] for indoor applications by eliminating the fourth-power terms, rearranging the factors, and introducing the exterior surface temperature of the building envelope as a variable. The resulting U-value formulation is expressed in Eq. 15:

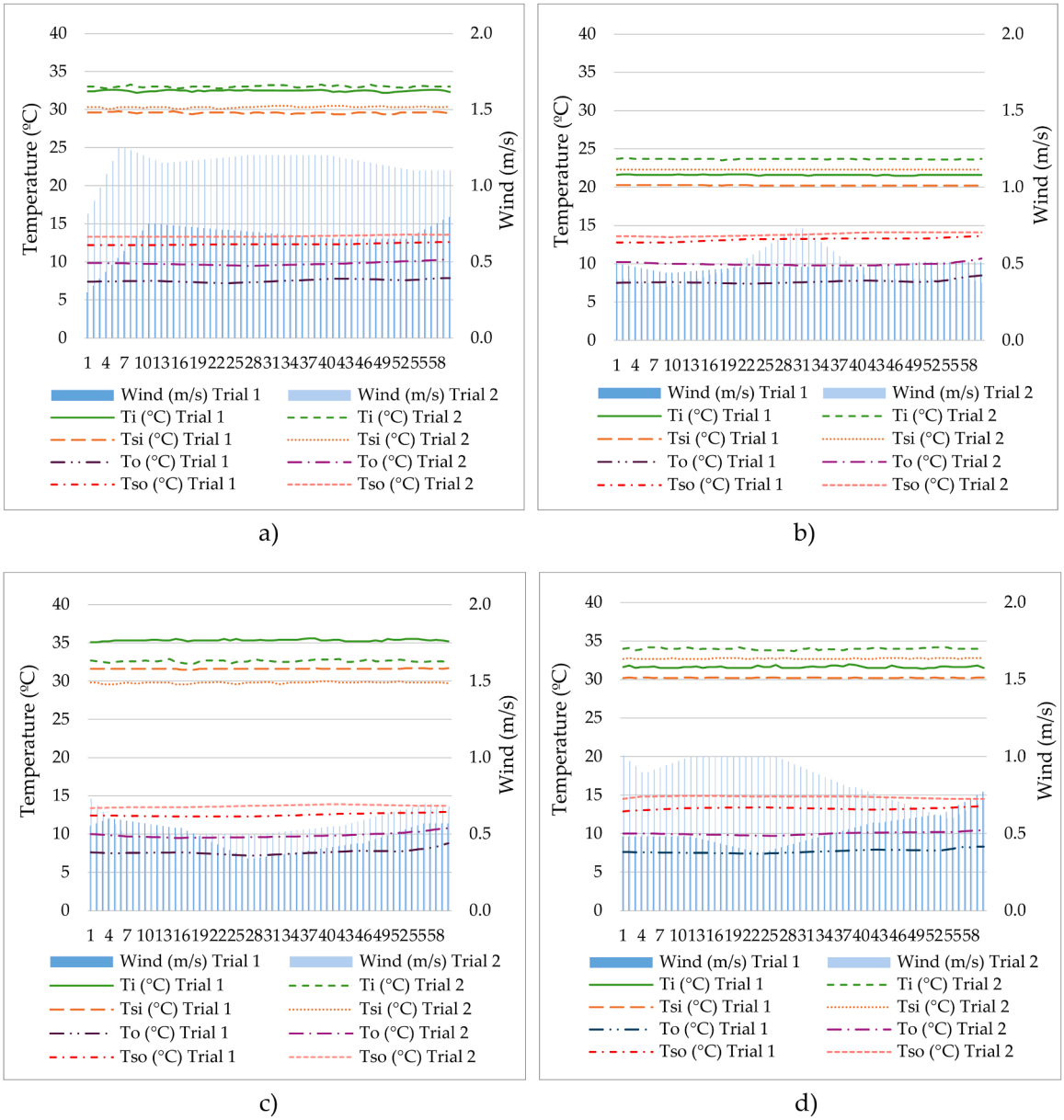

Fig. 5. Indoor and outdoor measurements: a) North façade, b) South façade, c) East façade, d) West façade.

$$U-value = \frac{\sigma\cdot\varepsilon\cdot\left(T_{ref}-T_{si}\right)+h_c\cdot\left(T_i-T_{si}\right)}{\left(T_{si}-T_{so}\right)}\frac{W}{m^2K} \quad (15)$$

Where T_{ref} is the environmental reflected temperature, and a standardized h_c value of 8.7 W/m^{2}K derived from Tanner et al [53] is used. Using this formulation, the authors found that emissivity and reflected temperature have no significant influence on the calculated U-value.

Finally, with the aim of evaluating the applicability and sensitivity of the proposed methods, the percentage deviation ($\Delta U_{\%}$) was determined using Eq. 16. This parameter quantifies the relative difference between U-values and was applied to:

(i) compare the U-values obtained using the different QIRT methods (U_{QIRT}) with the theoretical U-values (U_{THEOR})
(ii) assess the effect of façade orientation, taking the north façade as the reference; and
(iii) analyse the influence of boundary condition variations (ΔT_i, ΔT_{si}, ΔT_o, ΔT_{so} and Δv) by conducting an uncertainty analysis on the north façade that recalculated U-values under controlled perturbations of ±1 °C for temperatures and ±1 m/s for wind speed.

$$\Delta U_{\%} = \left(\frac{U_x-U_{ref}}{U_{ref}}\right)\cdot 100\% \quad (16)$$

Where U_x represents the U-value obtained under each condition (method, orientation, or boundary variation), and U_{ref} corresponds to the baseline U-value used for comparison.

3. Results

3.1. Measurement campaign

Fig. 5 summarizes the environmental conditions recorded before dawn during two winter trials. Trial 1 was colder ($T_o = 7.6$ °C) and less windy ($v = 0.5$– 0.7 m/s) than Trial 2 ($T_o = 9.9$ °C; $v < 1.2$ m/s), leading to a general rise in indoor (T_i) and surface temperatures (T_{si}, T_{so}) during the second campaign. T_i varied significantly by orientation: the south-facing room was consistently cooler (21.6– 23.7 °C), while the north, east, and west rooms reached markedly higher values (31.6– 35.3 °C). Surface temperatures followed a similar trend. T_{si} increased by 1– 2 °C in Trial 2, ranging from a minimum in the south (≈20– 22 °C) to maximums in the east and west (≈30– 33 °C). Outdoors, T_{so} rose by ≈1 °C on average, with the west and south façades consistently recording the highest temperatures (13.3– 14.7 °C) while the north remained the coldest (12.4– 13.3 °C).

3.2. U-value calculation

Table 4 summarizes the calculated U-values. The theoretical method consistently set the lower bound (0.47– 0.63 W/m^{2}K) across all orientations. In contrast, QIRT approaches exhibited significant variability (Fig. 6).

On the north façade, Methods A, B, and E yielded lower ranges (1.39–1.60 W/m^{2}K), whereas Method D and specifically Method C overestimated the value considerably, with the latter reaching up to 4.14 W/m^{2}K. The south façade exhibited the highest deviations. Method C recorded extreme values of 6.87– 11.67 W/m^{2}K, and Method D reached 4.95 W/m^{2}K. Only Method E remained within a lower range (1.41– 1.69 W/m^{2}K), diverging from the high overestimation trend of the other models. On the east façade, the pattern was similar to the north, Methods A, B and E ranged between 1.18–1.70 W/m^{2}K, while Method C reached 3.80 W/m^{2}K. Finally, on the west façade, Method C yielded values up to 4.89 W/m^{2}K, whereas Method E recorded 0.60–0.70 W/m^{2}K, remaining close to the theoretical calculation.

3.3. U-value uncertainty analysis

Table 5 summarizes the sensitivity analysis on the north façade. Regarding indoor air temperature (ΔT_i), most methods showed low sensitivity (A, B, and D within ±3.5– 5.1 %), except for Method E, which exhibited deviations up to ±35.8 % (Figures A.1a and A.1b). Variations in indoor surface temperature (ΔT_{si}) only affected Methods C and E: while C showed mild changes (<6.3 %), Method E experienced extreme deviations ranging from -39.3 % to +44.2 % (Figures A.1c and A.1d). Conversely, outdoor air temperature (ΔT_o) influenced all methods except E. Methods A, B, and D ranged from ±15.4 % to ±24.7 %, while Method C showed slightly higher sensitivity (up to ±27.6 %) (Figures A.1e and A.1f). For external surface temperature (ΔT_{so}), Method C was the most sensitive (from +32.3 % to -28.7 %), followed by the intermediate range of A, B, and D (±20.6– 28.1 %), with Method E being the most stable (±5.8 %) (Figures A.1 g and A.1 h). Finally, wind speed (Δv) caused the largest deviations for the methods incorporating it (A, B, D). Methods A and B were highly sensitive (increasing up to +41.5 % and +46.3 %, respectively), while Method D showed a moderate impact (+25 %) and Methods C and E remained unaffected (Figures A.1i and A.1j).

4. Discussion

4.1. Influence of façade orientation on the U-Value

The results demonstrated the critical influence of orientation on thermal transmittance. Using the north façade as a baseline, the south, east, and west façades exhibited higher U-values (+32 %, +21 %, and +34 %, respectively); this difference is attributed to the presence of an additional 2 cm layer of EPS insulation on the north façade. Experimental discrepancies were more pronounced. Regarding QIRT methods, the south façade presented the highest U-values (mean deviation +72 %), while the east and west façades showed values similar to the north (-6 % and +2 %). These findings are consistent with Ahmad et al. (2014), who reported higher heat fluxes in south, east, and west orientations, with differences of up to 37.3 % [54].

The differences between orientations are mainly attributed to uneven microclimatic conditions during measurements, accentuated by the use of separate rooms with independent HVAC systems. This resulted in indoor variations exceeding 10 °C: the south room remained cooler (≈21– 23 °C), while the north, east, and west rooms reached up to 35 °C. These differences reduced the indoor-outdoor thermal gradient (ΔT) in

Table 4
Average U-values calculated per façade and methodology.

Façade	Theoretical	U-Value (W/m^{2}K)									
		Trial 1					Trial 2				
		A	B	C	D	E	A	B	C	D	E
North	0.47	1.60	1.42	4.14	2.53	1.46	1.58	1.46	3.19	2.34	1.39
South	0.62	3.02	2.67	11.67	4.95	1.69	2.14	1.91	6.87	3.57	1.41
East	0.57	1.34	1.18	3.80	2.20	1.70	1.33	1.20	3.57	2.18	1.53
West	0.63	1.81	1.60	4.89	2.94	0.70	1.79	1.64	3.95	2.77	0.60

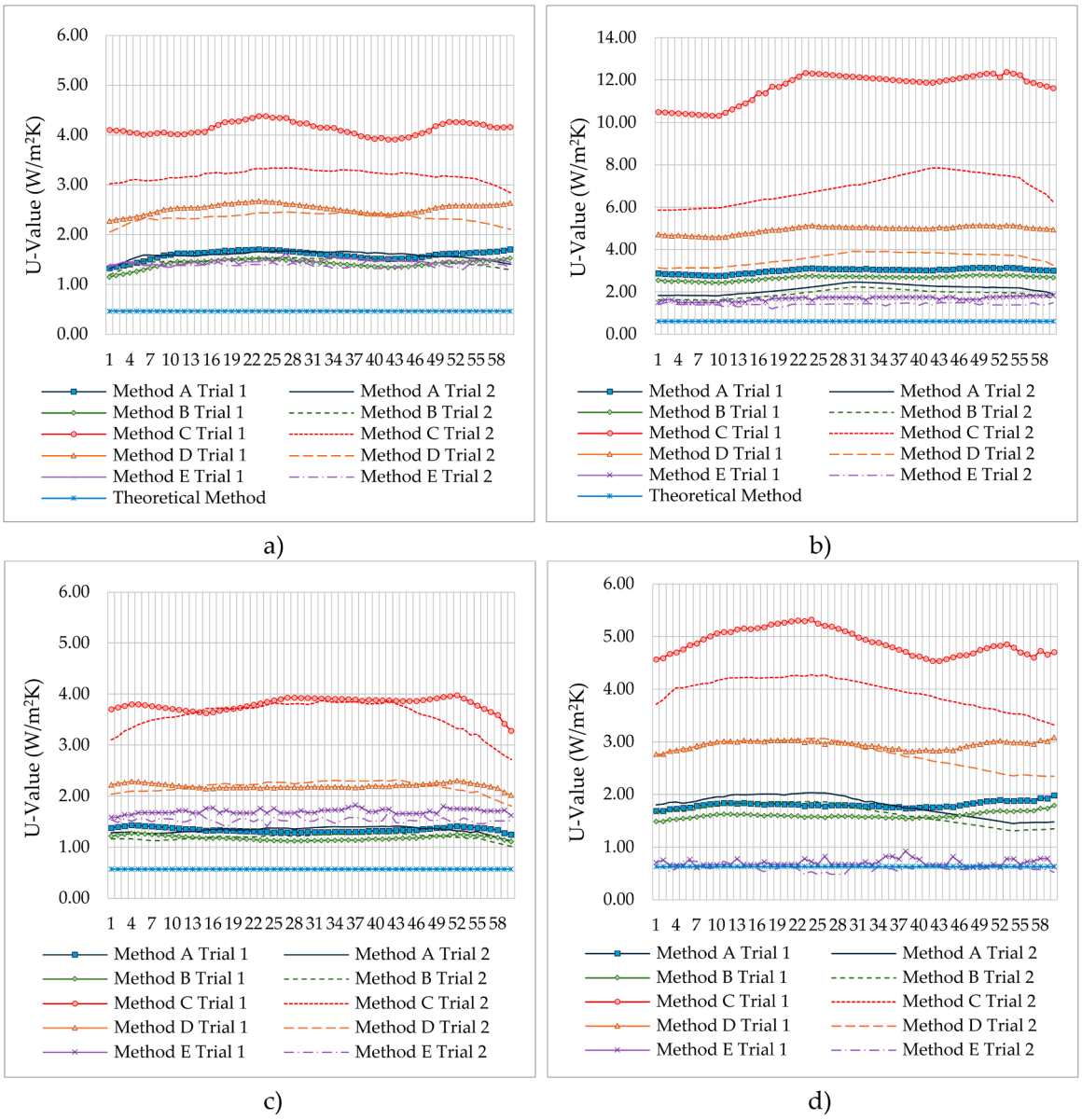

Fig. 6. U-values calculated per minute for each façade and methodology: a) North façade, b) South façade, c) East façade, d) West façade.

Table 5
Percentage deviations (ΔU %) calculated per methodology under controlled boundary condition variations.

ΔU-value $_{\%}$ (%)	Trial 1					Trial 2				
	A	B	C	D	E	A	B	C	D	E
Baseline (W/m^{2}K)	1.60	1.42	4.14	2.53	1.46	1.58	1.46	3.19	2.34	1.39
ΔU $_{\%}$ (ΔT_i = +1 °C)	-3.8	-3.5	0.0	-4.0	+34.9	-3.8	-4.1	0.0	-4.3	+36.7
ΔU $_{\%}$ (ΔT_i = -1 °C)	+4.4	+4.2	0.0	+4.0	-34.2	+5.1	+4.1	0.0	+4.7	-37.4
ΔU $_{\%}$ (ΔT_{si} = +1 °C)	0.0	0.0	-5.6	0.0	-37.7	0.0	0.0	-5.6	0.0	-41.0
ΔU $_{\%}$ (ΔT_{si} = -1 °C)	0.0	0.0	+6.3	0.0	+43.2	0.0	0.0	+6.3	0.0	+45.3
ΔU $_{\%}$ (ΔT_o = +1 °C)	-17.5	-16.9	-20.8	-17.0	0.0	-24.1	-24.7	-27.6	-23.5	0.0
ΔU $_{\%}$ (ΔT_o = -1 °C)	+16.3	+16.2	+20.8	+15.4	0.0	+22.8	+21.9	+27.6	+21.8	0.0
ΔU $_{\%}$ (ΔT_{so} = +1 °C)	+20.6	+21.8	+28.5	+20.9	+6.2	+27.8	+27.4	+36.1	+27.4	+5.8
ΔU $_{\%}$ (ΔT_{so} = -1 °C)	-20.6	-21.1	-25.4	-20.9	-5.5	-27.2	-28.1	-32.0	-27.4	-5.8
ΔU $_{\%}$ (Δv = +1 m/s)	+45.6	+52.1	0.0	+26.5	0.0	+37.3	+40.4	0.0	+23.5	0.0
ΔU $_{\%}$ (Δv = -1 m/s)	-30.0	-33.8	0.0	-17.8	0.0	-36.7	-40.4	0.0	-23.1	0.0

Table 6
Recommended QIRT methods for U-Value calculation based on sensitivity to boundary conditions.

Field Conditions and/or Measurement Limitation	Variables	Recommended Methods (Lower Sensitivity)	Methods to Avoid (Higher Sensitivity)
High Variability/Uncertainty in indoor air temperature	ΔT_i	A, B, C and D	E
High Variability/Uncertainty in internal surface temperature	ΔT_{si}	A, B, C and D	E
High Variability/Uncertainty in outdoor air temperature	ΔT_o	E	C
High Variability/Uncertainty in external surface temperature	ΔT_{so}	E	C
High Variability/Uncertainty in wind speed	Δv	C and E	A and B
Uncertain Conditions/Default Option	All variables	D	C

the south orientation, which may have contributed to the higher U-values observed on that façade.

The thermal behavior of the façades was conditioned by the interaction between solar radiation, outdoor temperature, and wind. The south and west façades recorded the highest surface temperatures due to solar gain, whereas the north façade remained cooler, an effect accentuated by wind (≈1.1 m/s), which increased convective losses. Wind is a critical factor, as it can introduce significant deviations in calculations; therefore, speeds below 2 m/s are recommended for in situ UAV-QIRT tests [55,56].

Consequently, the external thermal load influenced indoor boundary conditions via the wall's inertia. The south and west façades accumulated diurnal heat, thereby maintaining warmer internal surfaces during the night; this reduced the air-surface differential (≈1 °C) relative to the north and east orientations (≈3 °C). Such a reduced thermal gradient in sun-exposed façades compromises measurement accuracy and underscores the difficulty of achieving consistent results across all orientations.

4.2. Comparison between theoretical and experimental U-Values

The differences among methods stem from their distinct underlying assumptions, the specific mechanisms considered, the treatment of radiation, and the thermal reference used, all of which lead to variations in the resulting U-values. The theoretical method yielded the lowest values, serving as a static baseline. In contrast, experimental methods consistently overestimated this reference: Methods C and D showed the largest deviations (>284 %), Methods A and B were intermediate (>109 %), and Method E was the closest to the benchmark. This trend aligns with the literature, where in-situ measurements frequently exceed theoretical values by 14 % to 297 % [24,57–60]. These discrepancies are attributed to the overestimation of thermal properties and, above all, to the static nature of the theoretical calculation, which fails to reflect actual construction quality or the dynamic variability of environmental factors [61].

Regarding terrestrial QIRT (Methods A and B), previous studies report high sensitivity to environmental conditions with errors exceeding 150 % [43,45,46,62]. In this study, both overestimated the theoretical value, although Method B (1.18– 2.67 W/m^{2}K), which incorporates radiation, yielded slightly lower results than Method A (1.33– 3.02 W/m^{2}K) due to the convective coefficient employed. Method A proved highly sensitive to wind and convection, leading to larger overestimations under solar radiation or low thermal gradients.

For UAV-based methods (C, D, and E), literature reports deviations ranging from 20 % to 60 % for Methods C and E against theoretical and HFM values [44,47] identifying thermogram quality, viewing angle, and steady-state conditions as critical factors. Method D has shown variable errors of 3– 45 % relative to HFM measurements, with evidence that operational factors such as UAV distance, flight speed, and wind velocity directly reduce estimation reliability [48].

In this study, Method C proved extremely volatile (3.19– 11.67 W/m^{2}K), penalized by a denominator sensitive to low gradients and a high fixed convective coefficient. Method D also notably overestimated values (2.18– 4.95 W/m^{2}K) by integrating view factors and dynamic convection. Conversely, Method E (0.60– 1.70 W/m^{2}K) offered the closest agreement with theoretical values. However, this accuracy results from simplifying the formulation by removing the radiative term (T^4), which makes it similar to the THM method formula and highly dependent on indoor conditions [63].

Ultimately, the heterogeneity in the treatment of radiation (fourth-power terms vs. linearization) and convection (constant vs. wind-dependent coefficients) significantly alters the calculation. As concluded by Bienvenido-Huertas et al [64], the absence of a universal convective coefficient causes each method to amplify or attenuate the final result differently under identical thermal gradients.

4.3. Effect of boundary condition variations on the U-Value

The sensitivity analysis reveals that the algebraic formulation is the primary driver of each method's vulnerability, allowing for a categorization based on their critical dependency on specific input variables.

Methods A and B exhibit the study's largest deviations due to a critical dependency on the wind-dependent convective coefficient. With outdoor and indoor temperatures playing only secondary and tertiary roles respectively, these methods are practically unusable without precise, synchronous wind measurements. Method C is characterized by its volatility regarding external surface temperature, showing the highest deviation in this category. This instability stems from its denominator structure (surface temperature difference) which, combined with a high convective coefficient, leads to large overestimations. Consequently, it is advisable to avoid its use under fluctuating radiation or gusty wind conditions. Method E acts as an outlier driven by extreme sensitivity to internal surface temperature. While insensitive to wind and outdoor air temperature, and only marginally affected by outdoor surface temperature, its use is viable only if extremely accurate internal surface temperature measurements are guaranteed.

Method D is physically the most comprehensive, incorporating both convective and radiative terms, and displays a balanced sensitivity profile. While more stable against wind than Methods A and B, it remains vulnerable to outdoor temperature deviations. Consequently, it stands as the preferred default for uncertain conditions, provided sufficient boundary data is available.

From the sensitivity analysis to perturbations in the boundary conditions, it is observed that no single method is universally robust. The choice must prioritize the method with the lowest sensitivity to the variable with the highest uncertainty at the specific measurement site. Table 6 synthesizes these findings, providing a recommendation framework for selecting the appropriate QIRT method based on the availability and reliability of field boundary condition data.

4.4. Limitations

The use of UAV-mounted infrared thermography for quantitative analyses presents several operational and accuracy-related limitations.

The rotation of the UAV's propellers induces convection near the sensor, disturbing the Focal Plane Array (FPA) temperature and causing deviations in the measurement of the surface temperature (T_{so}), which requires an acclimatization period of at least 15 min before flight, significantly reducing the effective operational time due to limited battery autonomy [48,65].

In addition, flight speed and distance affect accuracy: it is recommended to fly at less than 0.5 m/s and at a distance of less than 15 m from the façade, as greater distances or higher speeds can distort the thermal image and reduce the reliability of the U-value [48]. Finally, the intrinsic accuracy of the IR sensor (±2 °C or ±2 %) can amplify errors, as deviations of ±20– 30 % in the U-values were observed when ΔT_{so} was varied by ±1 °C, significantly impacting the final U-value calculation.

5. Conclusions

This study evaluated the accuracy of various exterior and aerial thermography methodologies proposed in the literature for estimating thermal transmittance (U-value), applying them to the façades of a university building located in southwestern Spain. The results evidence that experimental variability among façades significantly exceeds theoretical expectations, confirming that each orientation must be analyzed as a specific case. In particular, the south façade exhibited U-values up to 72 % higher, a distortion attributed to heterogeneous microclimatic conditions and to operational differences in indoor climate control that altered the thermal gradient.

Compared to the static reference of the theoretical calculation (0.47–0.63 W/m^{2}K), in situ measurements showed a general tendency toward overestimation, driven by the intrinsic mathematical structure of each method. Methods A and B, developed for exterior thermography, yielded intermediate results; however, sensitivity analysis confirmed their high dependence on wind speed, resulting in deviations of up to 52 %. Methods C, D, and E, applied in UAV-based investigations, exhibited the widest dispersion. Method C proved the most unstable due to its extreme sensitivity to exterior surface temperature, whereas Method E achieved the closest approximation to theoretical values (+3 % to +203 %) due to formulaic simplifications that made it dependent on indoor conditions. Method D displayed a more balanced behavior, although its accuracy remains contingent on the quality of exterior measurements.

Overall, findings conclude that no universally robust UAV-QIRT method currently exists. The accuracy of current methodologies faces a structural technological barrier: the intrinsic ±2 °C or ±2 % uncertainty, characteristic of the infrared cameras currently available for UAV applications, together with the convective disturbances induced by UAV rotors, represents a significant barrier to achieving highly reliable QIRT results in the field. Consequently, to ensure the comparability of thermal assessments, future research must prioritize the development of more stable sensors and, fundamentally, the standardization of data acquisition protocols (distances, durations, and flight conditions).

Abbreviations

The following abbreviations are used in this manuscript:

QIRT	Quantitative Infrared Thermography
UAV	Unmanned Aerial Vehicle
ISO	International Organization for Standardization
HFM	Heat Flow Meter
THM	Thermometric Method
EPS	Expanded Polystyrene
CTE	Spanish Technical Building Code

Funding

This work has been supported by the project PID2023–146213OA-I00 funded by MCIN/AEI/10.13039/501100011033 and by "ERDF A way of making Europe".

Funding for open access charge

Universidad de Huelva / CBUA

CRediT authorship contribution statement

Marta Videras-Rodríguez: Writing – review & editing, Writing – original draft, Software, Methodology, Investigation, Formal analysis, Conceptualization. **Victoria Patricia López-Cabeza:** Writing – review & editing, Supervision, Data curation, Conceptualization. **Sergio Gómez-Melgar:** Writing – review & editing, Supervision, Resources, Project administration, Methodology, Investigation, Funding acquisition, Conceptualization. **José Manuel Andújar-Márquez:** Writing – review & editing, Validation, Supervision, Resources.

Declaration of competing interest

The authors declare the following financial interests/personal relationships which may be considered as potential competing interests:

Sergio Gomez Melgar reports financial support was provided by Spain Ministry of Science Innovation and Universities. If there are other authors, they declare that they have no known competing financial interests or personal relationships that could have appeared to influence the work reported in this paper.

Appendix A

Appendix A.1. Fig. A1.

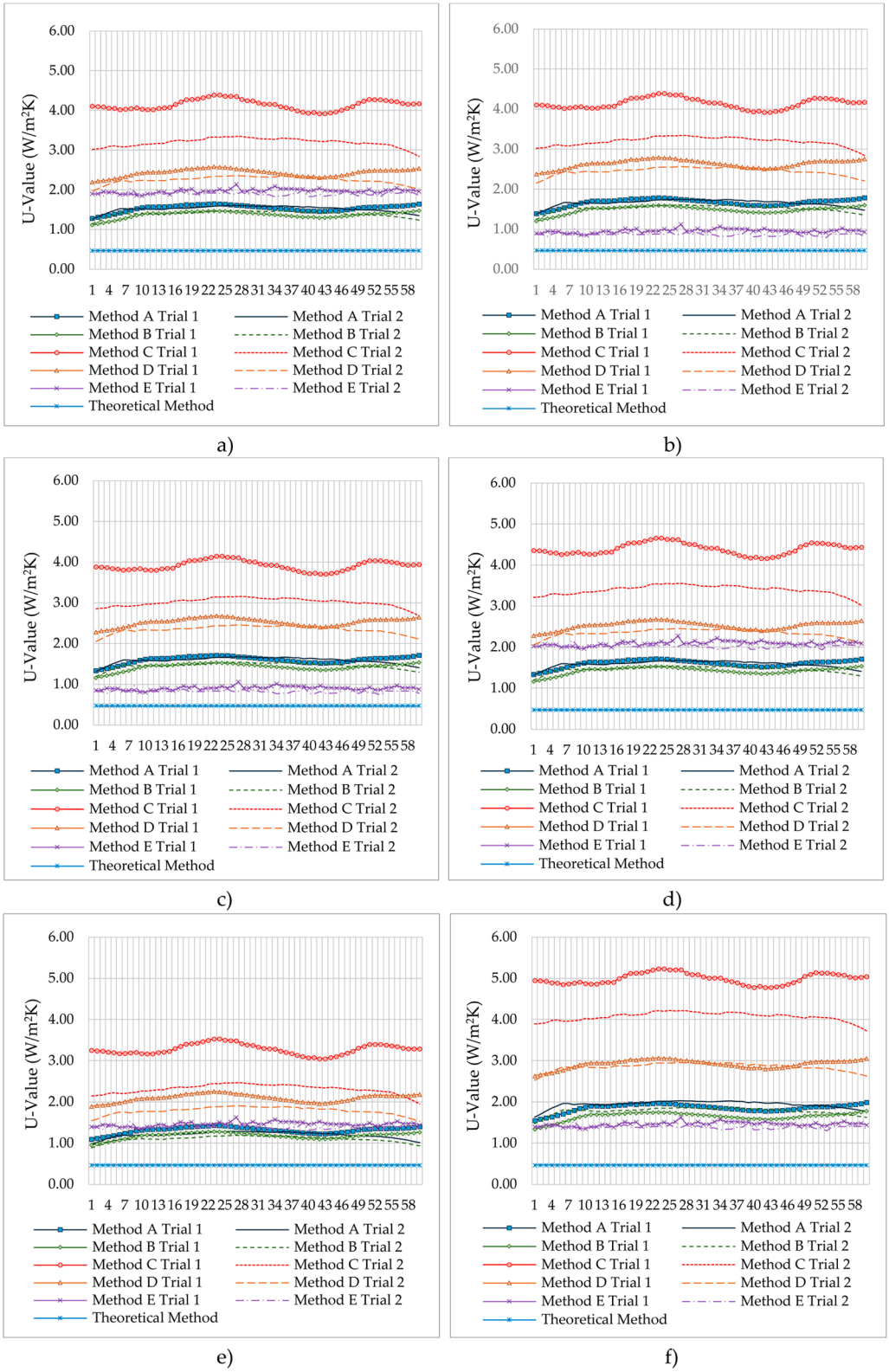

Fig. A1. U-values recalculated per modified variable and methodology: a) $\Delta T_i = +1$ °C, b) $\Delta T_i = -1$ °C, c) $\Delta T_{si} = +1$ °C, d) $\Delta T_{si} = -1$ °C, e) $\Delta T_o = +1$ °C, f) $\Delta T_o = -1$ °C, g) $\Delta T_{so} = +1$ °C, h) $\Delta T_{so} = -1$ °C, i) $\Delta v = +1$ m/s, j) $\Delta v = -1$ m/s.

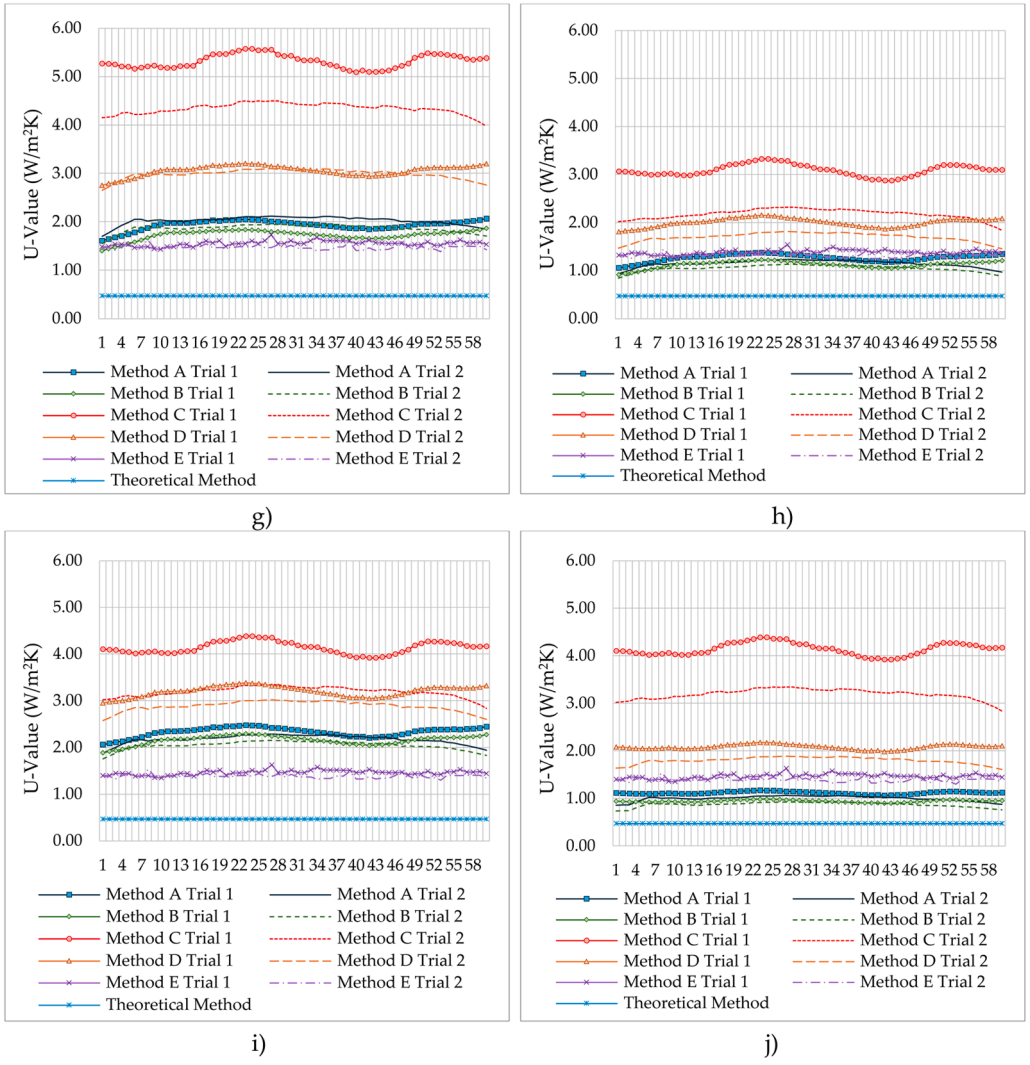

Fig. A1. (*continued*).

Data availability

Data will be made available on request.

References

[1] EPBD, Directive (EU) 2024 /1275 of the European Parliament and of the Council of 24 April 2024 on the energy performance of buildings, Off. J. Eur. Union 1275 (2024) 1–68. https://eur-lex.europa.eu/legal-content/EN/TXT/PDF/?uri=CELEX:52021DC0550&from=EN.

[2] European Commission, Energy Performance of Buildings Directive, 2025. https://energy.ec.europa.eu/topics/energy-efficiency/energy-performance-buildings/energy-performance-buildings-directive_en (accessed 8 October 2025).

[3] P. Biddulph, V. Gori, C.A. Elwell, C. Scott, C. Rye, R. Lowe, T. Oreszczyn, Inferring the thermal resistance and effective thermal mass of a wall using frequent temperature and heat flux measurements, Energy Build. 78 (2014) 10–16, https://doi.org/10.1016/j.enbuild.2014.04.004.

[4] G. Desogus, S. Mura, R. Ricciu, Comparing different approaches to in situ measurement of building components thermal resistance, Energy Build. 43 (2011) 2613–2620, https://doi.org/10.1016/j.enbuild.2011.05.025.

[5] T. Kalamees, Air tightness and air leakages of new lightweight single-family detached houses in Estonia, Build. Environ. 42 (2007) 2369–2377, https://doi.org/10.1016/j.buildenv.2006.06.001.

[6] M.A. Makawi, I.M. Budaiwi, A.A. Abdou, Characterization of envelope air leakage behavior for centrally air-conditioned single-Family detached houses, Buildings 13 (2023) 660, https://doi.org/10.3390/buildings13030660.

[7] Y. Hou, M. Chen, R. Volk, L. Soibelman, Investigation on performance of RGB point cloud and thermal information data fusion for 3D building thermal map modeling using aerial images under different experimental conditions, J. Build. Eng. 45 (2022) 103380, https://doi.org/10.1016/j.jobe.2021.103380.

[8] M. O'Grady, A.A. Lechowska, A.M. Harte, Infrared thermography technique as an in-situ method of assessing heat loss through thermal bridging, Energy Build. 135 (2017) 20–32, https://doi.org/10.1016/j.enbuild.2016.11.039.

[9] International Organization for Standardization, Thermal performance of buildings and building components — Physical quantities and definitions, ISO, Geneva, Switzerland, 2018. ISO Standard No. 7345:2018.

[10] International Organization for Standardization, Building components and building elements - Thermal resistance and thermal transmittance - Calculation methods, ISO 6946:2017, ISO, Geneva, Switzerland, 2017.

[11] J.M. Pérez-Bella, J. Domínguez-Hernández, E. Cano-Suñén, J.J. Del Coz-Díaz, F. P. Álvarez Rabanal, A correction factor to approximate the design thermal conductivity of building materials, Application to Spanish façades, Energy Build 88 (2015) 153–164, https://doi.org/10.1016/j.enbuild.2014.12.005.

[12] E. Lucchi, Thermal transmittance of historical stone masonries: A comparison among standard, calculated and measured data, Energy Build 151 (2017) 393–405, https://doi.org/10.1016/j.enbuild.2017.07.002.

[13] E. Lucchi, Thermal transmittance of historical brick masonries: A comparison among standard data, analytical calculation procedures, and in situ heat flow meter measurements, Energy Build 134 (2017) 171–184, https://doi.org/10.1016/j.enbuild.2016.10.045.

[14] A. Song, Y. Kim, S. Hwang, M. Shin, S. Lee, A comprehensive review of thermal transmittance assessments of building envelopes, Buildings 14 (2024) 1–28, https://doi.org/10.3390/buildings14103304.

[15] I. Nardi, E. Lucchi, In situ thermal transmittance assessment of the building envelope: practical advice and outlooks for standard and innovative procedures, Energies 16 (2023) 3319, https://doi.org/10.3390/en16083319.
[16] M. Teni, H. Krstić, P. Kosiński, Review and comparison of current experimental approaches for in-situ measurements of building walls thermal transmittance, Energy Build. 203 (2019) 0–17, https://doi.org/10.1016/j.enbuild.2019.109417.
[17] D. Bienvenido-Huertas, J. Moyano, D. Marín, R. Fresco-Contreras, Review of in situ methods for assessing the thermal transmittance of walls, Renew. Sustain. Energy Rev. 102 (2019) 356–371, https://doi.org/10.1016/j.rser.2018.12.016.
[18] N. Soares, C. Martins, M. Gonçalves, P. Santos, L.S. da Silva, J.J. Costa, Laboratory and in-situ non-destructive methods to evaluate the thermal transmittance and behavior of walls, windows, and construction elements with innovative materials: A review, Energy Build. 182 (2019) 88–110, https://doi.org/10.1016/j.enbuild.2018.10.021.
[19] M. Juaristi, M. Krarti, Review of adaptive opaque façades and laboratory tests for the dynamic thermal performance characterization, Build. Environ. 249 (2024) 111123, https://doi.org/10.1016/j.buildenv.2023.111123.
[20] International Organization for Standardization, Thermal insulation - Building elements - In-situ measurement of thermal resistance and thermal transmittance - Part 1: Heat flow meter method, ISO 9869-1:2014, ISO, Geneva, Switzerland, 2014.
[21] International Organization for Standardization, Thermal insulation - Building elements - In-situ measurement of thermal resistance and thermal transmittance - Part 2: Infrared method for frame structure dwellings, ISO 9869-2:2018, ISO, Geneva, Switzerland, 2018.
[22] D. Bienvenido-Huertas, R. Rodríguez-Álvaro, J.J. Moyano, F. Rico, D. Marín, Determining the U-value of fa ades using the thermometric method: potentials and limitations, Energies 11 (2018), https://doi.org/10.3390/en11020360.
[23] E. Genova, G. Fatta, The thermal performances of historic masonry: In-situ measurements of thermal conductance on calcarenite stone walls in Palermo, Energy Build. 168 (2018) 363–373, https://doi.org/10.1016/j.enbuild.2018.03.009.
[24] L. Evangelisti, C. Guattari, L. Fontana, R. De Lieto Vollaro, F. Asdrubali, On the ageing and weathering effects in assembled modular facades: On-site experimental measurements in an Italian building of the 1960s, J. Build. Eng. 45 (2022) 103519, https://doi.org/10.1016/j.jobe.2021.103519.
[25] G. Ficco, F. Iannetta, E. Ianniello, F.R. D'Ambrosio Alfano, M. Dell'Isola, U-value in situ measurement for energy diagnosis of existing buildings, Energy Build. 104 (2015) 108–121, https://doi.org/10.1016/j.enbuild.2015.06.071.
[26] B. Tejedor, M. Casals, M. Macarulla, A. Giretti, U-value time series analyses: evaluating the feasibility of in-situ short-lasting IRT tests for heavy multi-leaf walls, Build. Environ. 159 (2019) 106123, https://doi.org/10.1016/j.buildenv.2019.05.001.
[27] M. Videras-Rodriguez, S. Gomez-Melgar, A. Sánchez-Cordero, J.M. Andujar-Marquez, A critical review of unmanned aerial vehicles (UAVs) use in architecture and urbanism: scientometric and bibliometric analysis, Appl. Sci. 11 (2021) 9966, https://doi.org/10.3390/app11219966.
[28] T. Rakha, A. Gorodetsky, Review of Unmanned Aerial System (UAS) applications in the built environment: towards automated building inspection procedures using drones, Autom. Constr. 93 (2018) 252–264, https://doi.org/10.1016/j.autcon.2018.05.002.
[29] Z. Zhou, J. Irizarry, Y. Lu, A multidimensional framework for unmanned aerial system applications in construction project management, J. Manag. Eng. 34 (2018) 04018004, https://doi.org/10.1061/(asce)me.1943-5479.0000597.
[30] T.S.N. Rachmawati, S. Kim, Unmanned aerial vehicles (UAV) integration with digital technologies toward construction 4.0: A systematic literature review, Sustain. 14 (2022), https://doi.org/10.3390/su14095708.
[31] M. Videras-Rodriguez, S. Gomez-Melgar, J.M. Andujar-Marquez, Assessment of aerial thermography as a method of in situ measurement of radiant heat transfer in urban public spaces, Sustain. Cities Soc. 87 (2022) 104228, https://doi.org/10.1016/j.scs.2022.104228.
[32] M. Videras-Rodriguez, S. Gomez-Melgar, J.M. Andujar-Marquez, Design recommendations for the rehabilitation of an urban canyon in a subtropical climate region using aerial thermography and simulation tools, Energy Build. 298 (2023) 113525, https://doi.org/10.1016/j.enbuild.2023.113525.
[33] X. Wang, M.A. Rahman, M. Mokroš, T. Rötzer, N. Pattnaik, Y. Pang, Y. Zhang, L. Da, K. Song, The influence of vertical canopy structure on the cooling and humidifying urban microclimate during hot summer days, Landsc. Urban Plan. 238 (2023), https://doi.org/10.1016/j.landurbplan.2023.104841.
[34] D. Zhang, C. Zhan, L. Chen, Y. Wang, G. Li, Review of unmanned aerial vehicle infrared thermography (UAV-IRT) applications in building thermal performance: towards the thermal performance evaluation of building envelope, Quant. Infrared Thermogr. J. 22 (2025) 266–296, https://doi.org/10.1080/17686733.2024.2356913.
[35] T. Rakha, A. Liberty, A. Gorodetsky, B. Kakillioglu, S. Velipasalar, Heat mapping drones: an autonomous computer-vision-based procedure for building envelope inspection using unmanned aerial systems (UAS), Technol. Archit. Des. 2 (2018) 30–44, https://doi.org/10.1080/24751448.2018.1420963.
[36] Y. Hou, R. Volk, M. Chen, L. Soibelman, Fusing tie points' RGB and thermal information for mapping large areas based on aerial images: A study of fusion performance under different flight configurations and experimental conditions, Autom. Constr. 124 (2021) 103554, https://doi.org/10.1016/j.autcon.2021.103554.
[37] R. Madding, Finding R-values of stud frame constructed houses with IR thermography, Proc. ITC 126 (2008) 2008–2013.
[38] P.A. Fokaides, S.A. Kalogirou, Application of infrared thermography for the determination of the overall heat transfer coefficient (U-Value) in building envelopes, Appl. Energy 88 (2011) 4358–4365, https://doi.org/10.1016/j.apenergy.2011.05.014.
[39] B. Tejedor, M. Casals, M. Gangolells, X. Roca, Quantitative internal infrared thermography for determining in-situ thermal behaviour of façades, Energy Build. 151 (2017) 187–197, https://doi.org/10.1016/j.enbuild.2017.06.040.
[40] B. Tejedor, M. Casals, M. Gangolells, Assessing the influence of operating conditions and thermophysical properties on the accuracy of in-situ measured U-values using quantitative internal infrared thermography, Energy Build. 171 (2018) 64–75, https://doi.org/10.1016/j.enbuild.2018.04.011.
[41] A. Marshall, J. Francou, R. Fitton, W. Swan, J. Owen, M. Benjaber, Variations in the U-value measurement of a whole dwelling using infrared thermography under controlled conditions, Buildings 8 (2018), https://doi.org/10.3390/buildings8030046.
[42] I. Danielski, M. FrOling, Diagnosis of buildings' thermal performance-a quantitative method using thermography under non-steady state heat flow, Energy Proc. 83 (2015) 320–329, https://doi.org/10.1016/j.egypro.2015.12.186.
[43] G. Dall'O', L. Sarto, A. Panza, Infrared screening of residential buildings for energy audit purposes: results of a field test, Energies 6 (2013) 3859–3878, https://doi.org/10.3390/en6083859.
[44] N. Bayomi, S. Nagpal, T. Rakha, J.E. Fernandez, Building envelope modeling calibration using aerial thermography, Energy Build. 233 (2021) 110648, https://doi.org/10.1016/j.enbuild.2020.110648.
[45] R. Albatici, A.M. Tonelli, Infrared thermovision technique for the assessment of thermal transmittance value of opaque building elements on site, Energy Build. 42 (2010) 2177–2183, https://doi.org/10.1016/j.enbuild.2010.07.010.
[46] R. Albatici, A.M. Tonelli, M. Chiogna, A comprehensive experimental approach for the validation of quantitative infrared thermography in the evaluation of building thermal transmittance, Appl. Energy 141 (2015) 218–228, https://doi.org/10.1016/j.apenergy.2014.12.035.
[47] A. Benz, J. Taraben, P. Debus, B. Habte, L. Oppermann, N. Hallermann, C. Voelker, V. Rodehorst, G. Morgenthal, Framework for a UAS-based assessment of energy performance of buildings, Energy Build 250 (2021) 111266, https://doi.org/10.1016/j.enbuild.2021.111266.
[48] D. Zhang, C. Zhan, L. Chen, Y. Wang, G. Li, An in-situ detection method for assessing the thermal transmittance of building exterior walls using unmanned aerial vehicle–infrared thermography (UAV-IRT), J. Build. Eng. 91 (2024) 109724, https://doi.org/10.1016/j.jobe.2024.109724.
[49] M.C. Peel, B.L. Finlayson, T.A. McMahon, Updated world map of the Köppen-Geiger climate classification, Hydrol. Earth Syst. Sci. 11 (2007) 1633–1644, https://doi.org/10.5194/hess-11-1633-2007.
[50] X. Zhong, L. Zhao, P. Ren, R. Wu, X. Zhang, Z. Shen, J. Yan, The role of UAV-derived multimodal images in outdoor thermal comfort observation, evaluation, and improvement: A case study in Guangzhou, Sustain. Cities Soc. 131 (2025) 106723, https://doi.org/10.1016/j.scs.2025.106723.
[51] International Organization for Standardization, Condition monitoring and diagnostics of machines - Thermography - Part 1: General procedures, ISO 18434-1:2008, ISO, Geneva, Switzerland, 2008.
[52] K. Watanabe, Architectural Planning Fundamentals Maruzen, Tokyo, 1965.
[53] C. Tanner, B. Lehmann, T. Frank, K.G. Wakili, A proposal for standardized thermal images, Bauphysik 33 (2011) 345–356, https://doi.org/10.1002/bapi.201110801.
[54] A. Ahmad, M. Maslehuddin, L.M. Al-Hadhrami, In situ measurement of thermal transmittance and thermal resistance of hollow reinforced precast concrete walls, Energy Build. 84 (2014) 132–141, https://doi.org/10.1016/j.enbuild.2014.07.048.
[55] F. Wang, D. Wang, X. Wang, J. Yao, A data analysis method for detecting wall thermal resistance considering wind velocity in situ, Energy Build. 42 (2010) 1647–1653, https://doi.org/10.1016/j.enbuild.2010.04.007.
[56] B. Lehmann, K. Ghazi Wakili, T. Frank, B. Vera Collado, C. Tanner, Effects of individual climatic parameters on the infrared thermography of buildings, Appl. Energy 110 (2013) 29–43, https://doi.org/10.1016/j.apenergy.2013.03.066.
[57] L. Evangelisti, C. Guattari, R. De Lieto Vollaro, F. Asdrubali, A methodological approach for heat-flow meter data post-processing under different climatic conditions and wall orientations, Energy Build. 223 (2020) 110216, https://doi.org/10.1016/j.enbuild.2020.110216.
[58] F. Asdrubali, F. D'Alessandro, G. Baldinelli, F. Bianchi, Evaluating in situ thermal transmittance of green buildings masonries: A case study, Case Stud, Constr. Mater. 1 (2014) 53–59, https://doi.org/10.1016/j.cscm.2014.04.004.
[59] L. Evangelisti, C. Guattari, P. Gori, R. De Lieto Vollaro, In situ thermal transmittance measurements for investigating differences between wall models and actual building performance, Sustain. 7 (2015) 10388–10398, https://doi.org/10.3390/su70810388.
[60] R. O'Hegarty, O. Kinnane, D. Lennon, S. Colclough, In-situ U-value monitoring of highly insulated building envelopes: review and experimental investigation, Energy Build. 252 (2021) 111447, https://doi.org/10.1016/j.enbuild.2021.111447.

[61] S.I. Kim, J.S. Choi, J.H. Jo, J. Joe, Y.H. Cho, E.J. Kim, Simulation-based comparative analysis of U-value of field measurement methods, Case Stud, Therm. Eng. 50 (2023) 103433, https://doi.org/10.1016/j.csite.2023.103433.
[62] I. Nardi, D. Paoletti, D. Ambrosini, T. De Rubeis, S. Sfarra, U-value assessment by infrared thermography: A comparison of different calculation methods in a guarded Hot box, Energy Build. 122 (2016) 211–221, https://doi.org/10.1016/j.enbuild.2016.04.017.
[63] M. Videras-Rodriguez, S. Gomez-Melgar, J.M. Andujar-Marquez, Evaluation of aerial thermography for measuring the thermal transmittance (U-value) of a building façade, Energy Build. 324 (2024), https://doi.org/10.1016/j.enbuild.2024.114874.
[64] D. Bienvenido-Huertas, J. Bermúdez, J. Moyano, D. Marín, Comparison of quantitative IRT to estimate U-value using different approximations of ECHTC in multi-leaf walls, Energy Build. 184 (2019) 99–113, https://doi.org/10.1016/j.enbuild.2018.11.028.
[65] M. Mahmoodzadeh, V. Gretka, P. Mukhopadhyaya, Challenges and opportunities in quantitative aerial thermography of building envelopes, J. Build. Eng. 69 (2023) 106214, https://doi.org/10.1016/j.jobe.2023.106214.